ACADEMIC PRESS

Available online at www.sciencedirect.com

SCIENCE DIRECT®

Journal of Sound and Vibration 260 (2003) 671–691

JOURNAL OF SOUND AND VIBRATION

www.elsevier.com/locate/jsvi

An analytical and experimental comparison of optimal actuator and error sensor location for vibration attenuation

Nicole J. Kessissoglou[a,*], Patrik Ragnarsson[b], Anders Löfgren[b]

[a] *School of Engineering, James Cook University, Townsville, Qld. 4811, Australia*

[b] *Marcus Wallenberg Laboratory for Sound and Vibration Research, KTH, 100 44 Stockholm, Sweden*

Received 19 June 2001; accepted 8 May 2002

Abstract

Feedforward active control of the flexural waves in a single and L-shaped plate has been analytically and experimentally investigated. The plates are simply supported along two parallel edges, and free at the other two ends. Point forces were used to generate the primary and secondary plate excitations. The plate flexural displacement is described by a combination of a travelling wave solution and a modal expansion. The flexural wave coefficients were determined using the boundary conditions, continuity equations at the driving force locations, and continuity equations at the corner junction for the L-shaped plate. The control actuator and error sensor are optimally located in order to achieve the best control performance.

1. Introduction

Active control of large distributed structures has attracted considerable interest in the last decade, where such structures are commonly found in the aerospace and marine industries. With significant progress in control techniques, signal processing and adaptive materials, the successful implementation of active control technology is becoming a reality. Much research has been focused on actively attenuating the structural and acoustic fields associated with beams, plates and cylindrical shells. Application of multiple actuators and error sensors for reduction of the power flow has been investigated for a semi-infinite plate [1]. The control actuators and error sensors are located downstream of the primary forces. It was shown that when only a single control actuator was used, its optimal location was strongly dependent on frequency. Increasing the number of control actuators resulted in an increase in the vibratory power transmission

*Corresponding author. Tel.: +617-4781-5082; fax: +617-4781-4660.
E-mail address: nicole.kessissoglou@jcu.edu.au (N.J. Kessissoglou).

0022-460X/03/$ - see front matter
PII: S0022-460X(02)00987-2

reduction. Active control of the structural fields to attenuate the sound radiation from a simply supported plate mounted in a rigid steel frame has been experimentally examined [2]. The number and position of the piezoelectric actuators were varied in order to examine the effect on distributed control. From the experimental study, the following important results were obtained: (i) increasing the number of control actuators only slightly improved attenuation at a structural resonance; (ii) the actuator location greatly affected the structural response. Similar work on a semi-infinite beam with a clamped edge verified that the attenuation is dependent on the actuator position rather than on the type of actuator [3]. Methods for optimising the locations of the error sensors and control actuators in an active control system include the use of genetic algorithms [4] and gradient methods [5]. Although there has been much research in wave transmission in L-shaped plates [6–8], there has been very little work on the active vibration control of coupled plate structures [9].

In this paper, an analytical and experimental investigation on optimising the error sensor and control force locations with respect to the primary force location is presented. When a single control source and a single error sensor are both optimally located with respect to the primary force location in a symmetrical arrangement, the control performance at single frequencies over a broad frequency range becomes optimised and independent of the excitation frequency. Under single frequency control, the use of single and multiple number of error sensors are examined to determine their control effect on the global response of the plate. To evaluate and compare the global response of the plate for various error sensor locations, the time-averaged kinetic energy was calculated. Experimental work has been conducted to confirm the analytical results.

2. Theory

The single rectangular thin plate is simply supported at $y = 0$ and L_y and free at $x = 0$ and L_x. The L-shaped plate consists of two finite plates coupled together at a right angle, and is simply supported at $y = 0$ and L_y, and free at the other two ends corresponding to $x_1 = L_{x1}$ and $x_2 = L_{x2}$. The junction of the two plates corresponds to $x_1 = 0$ and $x_2 = 0$. Point force excitation of the single and coupled plates at a location of (x_p, y_p) is used to model the vertically mounted primary shaker used in the experiments. Due to the boundary conditions, the plate flexural displacement can be described by both a modal expansion in the y direction, and a travelling wave solution along the x direction. General solutions for the primary plate flexural displacement can be described by [1,9]

$$W_j^p(x,y) = F_p G_p, \quad \text{where } G_p = \sum_{m=1}^{\infty} \frac{2}{L_y D} \sin(k_y y_p)\,[\alpha_p]_{n,8}^{-1}\,[E_j^p]\sin(k_y y). \tag{1}$$

The subscript 'j' corresponds to $j = 1, 2$ for the single plate, and $j = 1$ to 3 for the L-shaped plate. For the single plate, $[E_j^p]$ is given by

$$[E_1^p] = [\,\mathrm{e}^{-\mathrm{j}k_x x} \quad \mathrm{e}^{\mathrm{j}k_x x} \quad \mathrm{e}^{-k_n x} \quad \mathrm{e}^{k_n x} \quad 0 \quad 0 \quad 0 \quad 0\,]^{\mathrm{T}}, \quad 0 \leqslant x \leqslant x_p, \tag{2}$$

$$[E_2^p] = [\,0 \quad 0 \quad 0 \quad 0 \quad \mathrm{e}^{-\mathrm{j}k_x x} \quad \mathrm{e}^{\mathrm{j}k_x x} \quad \mathrm{e}^{-\mathrm{k}_n x} \quad \mathrm{e}^{\mathrm{k}_n x}\,]^{\mathrm{T}}, \quad x_p \leqslant x \leqslant L_x \tag{3}$$

and for the L-shaped plate, $[E_j^p]$ is given by

$$[E_1^p] = [\mathrm{e}^{-\mathrm{j}k_{x1}x_1} \quad \mathrm{e}^{\mathrm{j}k_{x1}x_1} \quad \mathrm{e}^{-k_{n1}x_1} \quad \mathrm{e}^{k_{n1}x_1} \quad 0 \quad 0 \quad 0 \quad 0 \quad 0 \quad 0 \quad 0 \quad 0]^{\mathrm{T}}, \quad L_{x1} \leqslant x_1 \leqslant x_p, \tag{4}$$

$$[E_2^p] = [0 \quad 0 \quad 0 \quad 0 \quad \mathrm{e}^{-\mathrm{j}k_{x1}x_1} \quad \mathrm{e}^{\mathrm{j}k_{x1}x_1} \quad \mathrm{e}^{-k_{n1}x_1} \quad \mathrm{e}^{k_{n1}x_1} \quad 0 \quad 0 \quad 0 \quad 0]^{\mathrm{T}}, \quad x_p \leqslant x_1 \leqslant 0, \tag{5}$$

$$[E_3^p] = [0 \quad 0 \quad 0 \quad 0 \quad 0 \quad 0 \quad 0 \quad 0 \quad \mathrm{e}^{-\mathrm{j}k_{x2}x_2} \quad \mathrm{e}^{\mathrm{j}k_{x2}x_2} \quad \mathrm{e}^{-k_{n2}x_2} \quad \mathrm{e}^{k_{n2}x_2}]^{\mathrm{T}}, \quad 0 \leqslant x_2 \leqslant L_{x2}. \tag{6}$$

In the analytical modelling of the L-shaped plate, x_1, x_p and L_{x1} correspond to negative values. $[\alpha_p]$ is an 8×8 matrix for the single plate, and is given in Appendix A. For the L-shaped plate, $[\alpha_p]$ corresponds to a 12×12 matrix, as shown in Appendix B. These matrices were developed using the boundary conditions at the free edges [10], continuity equations at the driving forced location [1], and continuity equations at the structural junction of the L-shaped plate [9]. $[\alpha]_{n,8}^{-1}$ corresponds to the eighth column of the inverse of matrix $[\alpha_p]$, where $n = 1, \ldots, 8$ for the single plate, and $n = 1, \ldots, 12$ for the L-shaped plate.

3. Active control

A single point control force of amplitude F_s is used to generate secondary excitation at a location of (x_s, y_s) in the plates. Expressions for the secondary flexural displacement can be obtained in the same way as for the primary displacement, resulting in

$$W_j^s(x, y) = F_s G_s, \quad \text{where } G_s = \sum_{m'=1}^{\infty} \frac{2}{L_y D} \sin(k_y y_s)[\alpha_s]_{n,8}^{-1}[E_j^s]\sin(k_y y). \tag{7}$$

$[E_j^s]$ is similar to Eqs. (2)–(6), but is instead a function of m', and with x_p replaced by x_s. Likewise, $[\alpha_s]$ is also similar to $[\alpha_p]$, but with the same replacements. The total flexural displacement is the superposition of the primary flexural waves generated by the primary force, and the secondary flexural waves generated by the control force, that is

$$W_j^{total}(x, y) = W_j^p(x, y) + W_j^s(x, y). \tag{8}$$

3.1. Minimisation of the cost function using a single error sensor

The total squared displacement is the cost function to be minimised at a single error sensor location in the plates. For the L-shaped plate, the error sensor is located in the adjacent plate in order to minimise the flexural wave transmission. Using Eqs. (1), (7) and (8), the total squared plate displacement at an error sensor location of (x_e, y_e) can be expressed as a quadratic function of the control force by

$$\Pi = W_j^{total}(W_j^{total})^* = F_s A_\Pi F_s^* + F_s^* B_\Pi F_p + F_s B_\Pi^* F_p^* + F_p^* C_\Pi F_p, \tag{9}$$

where $A_\Pi = G_s G_s^*$, $B_\Pi = G_s^* G_p$ and $C_\Pi = G_p^* G_p$. Due to orthogonality relationships of modes, A_Π is a function of mode number m', whereas B_Π and C_Π are functions of m. The unique minimum of the cost function results in the optimal control force amplitude. This is determined from the solution of the two equations corresponding to the partial derivatives of the cost function with

respect to the real and imaginary parts of the control force [11]. The optimal control force resulting in the minimum squared plate displacement is obtained as

$$F_s|_{opt} = -F_p \frac{B_\Pi}{A_\Pi}. \tag{10}$$

3.2. Minimisation of the cost function using multiple error sensors

Multiple error sensors are used in the active control application, and are located at (x_{ei}, y_{ei}) for $i = 1, \ldots, N$. The cost function now becomes the sum of the total squared plate displacement due to the primary and control forces for every error sensor location, and is expressed as

$$\Pi = \sum_{i=1}^{N} (W_j^{total}(x_{ei}, y_{ei}))(W_j^{total}(x_{ei}, y_{ei}))^* = F_s A_\Pi F_s^* + F_s^* B_\Pi F_p + F_s B_\Pi^* F_p^* + F_p^* C_\Pi F_p, \tag{11}$$

where

$$A_\Pi = \sum_{i=1}^{N} G_s(x_{ei}, y_{ei})(G_s(x_{ei}, y_{ei}))^*, \tag{12}$$

$$B_\Pi = \sum_{i=1}^{N} G_p(x_{ei}, y_{ei})(G_s(x_{ei}, y_{ei}))^*, \tag{13}$$

$$C_\Pi = \sum_{i=1}^{N} G_p(x_{ei}, y_{ei})(G_p(x_{ei}, y_{ei}))^*. \tag{14}$$

The optimal control force resulting in the minimum squared displacement at the N error sensor locations is still obtained as $F_s|_{opt} = -F_p B_\Pi / A_\Pi$.

3.3. Plate kinetic energy

To evaluate and compare the global attenuation of the plate for various error sensors locations, the total kinetic energy of the plate was calculated. The total time-averaged vibrational kinetic energy for a single resonance frequency can be written as [11]

$$E_k(\omega) = \frac{M\omega^2}{4} [\mathbf{A}]^{\mathrm{H}} [\mathbf{A}], \tag{15}$$

where M is the total mass of the plate, $[\mathbf{A}]$ is the coefficient matrix of the plate displacement, and the superscript H denotes the complex conjugate and transpose. The coefficient matrix under primary excitation can be written as $[\mathbf{A}] = [\alpha_p]_{n,8}^{-1}(2F_p/L_y D)\sin(k_y y_p)$, and under secondary excitation, the subscript p is replaced by s.

4. Experimental arrangement

The experimental rig consisted initially of a single aluminium test panel of thickness $h = 0.002\,\mathrm{m}$, length $L_x = 1.4\,\mathrm{m}$ and width $L_y = 0.5\,\mathrm{m}$. The boundaries of the plate were

constructed to simulate the simply supported conditions on two parallel sides of the plate, and free conditions on the other two ends. The simply supported boundary conditions of the panel were implemented by using strips of 0.9 mm thick aluminium cut into Z-sections [12]. The primary and secondary mini shakers were mounted vertically over the plate in order to model the point force excitation and generate flexural vibration in the plate. An EZ-ANC controller which is based on an adaptive filtered-X LMS algorithm was used for the active control experiments [13]. Brüel & Kjær Type 4375 miniature accelerometers were used as the error sensors, and were attached to the plate with beeswax. Two accelerometers were used for the minimisation of the cost function using multiple error sensors. A third accelerometer was used to map the surface response of the plate in both the uncontrolled and controlled experiments. In order to map the surface response, the plate was meshed into 140 squares with 135 grid points over the surface. The mesh gave an adequate number of points to obtain the surface response for lower order modes. In the experiments, the total kinetic energy of the plate at a single frequency was evaluated by $E_k(\omega) = (\rho h/2\omega^2)\sum_{k=1}^{135} a_k^2 \Delta S_k$, where a_k is the measured acceleration at a certain measurement point and ΔS_k is the corresponding area for that measuring point. Stability in the control application and system response was observed for each location of the mapping accelerometer. This was achieved by observing the uncontrolled and controlled acceleration responses at an error sensor location and the mapping accelerometer location. The two locations were simultaneously observed in the Brüel & Kjær Type 2034 Dual Channel Signal Analyser. The measured responses at the error sensor location deviated by less than 0.2 dB.

For the L-shaped plate rig, a second aluminium plate was welded to the original plate at a right angle. The second plate of length $L_{x2} = 0.6$ m, and equal thickness and width to the original plate, was also simply supported on two parallel sides and free at the two ends parallel to the corner junction. The total number of grid points of the L-shaped plate was 198, and the mesh had the same resolution as in the single plate. Fig. 1 shows a photograph of the L-plate experimental rig and the mounted shakers.

5. Results and discussion

5.1. Single plate: excitation and control at single frequencies over a broad frequency range

The effect of the control force and error sensor locations in the control performance was analytically investigated at single frequencies over a broad frequency range. The material properties of the aluminium plate used in the analytical modelling are $\rho = 2800\,\mathrm{kg/m^3}$, $E = 7.1 \times 10^{10}\,\mathrm{N/m^2}$ and $\upsilon = 0.3$. The internal distributed damping in the plates was included in the complex Young's modulus by $\tilde{E} = E(1 + \mathrm{j}\eta)$, where $\eta = 0.001$. Initial investigation of the effect of the error sensor location on the control performance was conducted for fixed primary and control force locations. The shaker and accelerometer locations are given in metres. A fixed primary shaker location of $(x_p, y_p) = (0.6, 0.19)$ was chosen, where $y_p = 0.618L_y = 0.19$ m corresponds to a structural location which results in excitation of all modes. For a control shaker location of $(x_s, y_s) = (0.8, 0.31)$, several error sensor positions were examined. It was initially revealed that the y_e co-ordinate of the error sensor affected the control performance significantly greater than the x_e co-ordinate, provided that the error sensor is positioned some

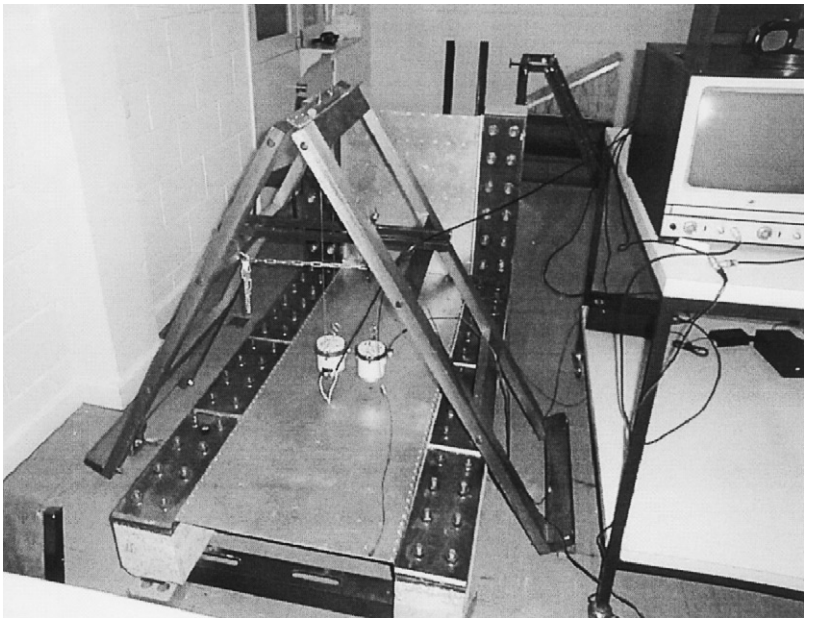

Fig. 1. Photograph of the L-plate experimental rig showing the boundary conditions and the vertically mounted primary and control shakers.

distance downstream of the actuators, thus avoiding the flexural near-field effects. Fig. 2 shows the uncontrolled frequency response function of the plate obtained analytically. The controlled acceleration distributions for two different error sensor locations are also shown. The controlled response corresponds to tonal frequency control at each excitation frequency over a broad frequency range. The error sensor locations correspond to $(x_{e1}, y_{e1}) = (1.1, 0.19)$, which is in-line with the primary force along the x direction, and $(x_{e2}, y_{e2}) = (1.1, 0.25)$, which is midway between the primary and control forces in the y direction. Similar controlled results were obtained when the single error sensor was located in-line with either the primary force or the control force along the x direction. This can be attributed to the symmetrical arrangement of the forces in the y direction.

The effect of the control force location was then investigated for a fixed error sensor location. For the same primary shaker location of $(x_p, y_p) = (0.6, 0.19)$, and a fixed error sensor location of $(x_e, y_e) = (1.1, 0.25)$, three control force locations were examined. These correspond to $(x_{s1}, y_{s1}) = (0.8, 0.19)$, which is in line with the primary force in the x direction, $(x_{s2}, y_{s2}) = (0.6, 0.25)$ which is both in line with the primary force in the y direction and in line with the error sensor in the x direction, and $(x_{s3}, y_{s3}) = (0.6, 0.31)$, which is both in line with the primary force and symmetrical about the error sensor location in the y direction. Fig. 3 shows that the optimal location for the control force of the three locations corresponds to (x_{s3}, y_{s3}), that is, when the control force is in line with the primary force in the y direction, and the error sensor is located midway between and downstream of the two shakers. When the locations of the control force and the error sensor are not optimised with respect to the primary source location, the control performance is strongly dependent on the excitation frequency, that is, greater attenuation is achieved at some frequencies

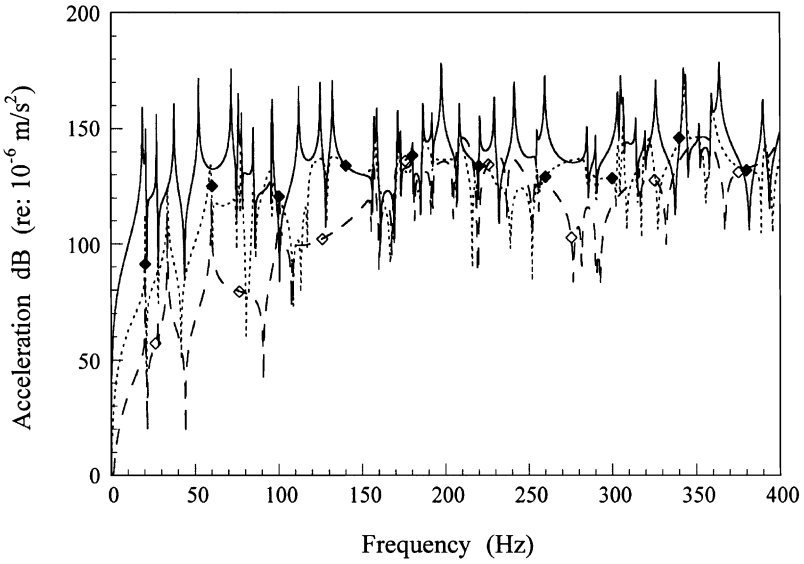

Fig. 2. Primary (——) and controlled acceleration distributions for single frequency control over a broad frequency range at fixed primary and control force locations of (0.6,0.19) and (0.8,0.31), respectively, and error sensor locations of (1.1,0.19) (- - - - ◆ - - -) and (1.1,0.25) ((- ◇ -)).

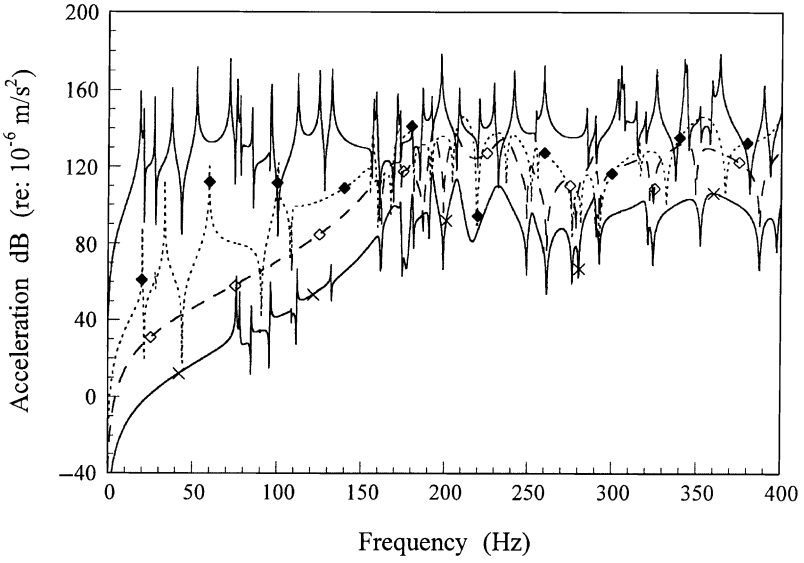

Fig. 3. Primary (——) and controlled acceleration distributions for single frequency control over a broad frequency range at a fixed primary force and error sensor locations of (0.6,0.19) and (1.1,0.25), respectively, and control force locations of (0.8,0.19) (- - - - ◆ - - -), (0.6,0.25) ((- ◇ -)) and (0.6,0.31) ((—×—)).

than others. However, when both the control force and error sensor locations are optimised, global attenuation is achieved at all frequencies, and the control performance is frequency independent. The symmetrical arrangement of the optimal control application for tonal frequency

control can be attributed to the simply supported boundary conditions at $y = 0$ and L_y. With the symmetrical control arrangement, the control force and error sensor will, respectively, excite and observe/attenuate the same set of modes. The corresponding optimal control force amplitudes are shown in Fig. 4. An interesting observation is that the corresponding optimal control force amplitude is unity for all frequencies. For control force locations away from the optimal location, a large force amplitude is required at certain discrete resonance frequencies in order to attenuate the plate response at the error sensor location.

Under the symmetrical control application, the control performance becomes maximised and independent of the excitation frequency. Fig. 5 shows the uncontrolled and controlled responses using the symmetrical control arrangement for a frequency span up to 10 kHz. From the figure, it is evident that the control performance is optimised and frequency independent. Under this optimal control application, the corresponding control force amplitude is always unity.

5.2. Single plate: single frequency control using a single error sensor

Optimal actuator and error sensor locations at a single resonance frequency were then investigated in order to achieve global attenuation of the plate vibration. Since the EZ-ANC controller used in the experiments has its best performance in the frequency range from 200 to 500 Hz, a low resonance frequency of 209 Hz obtained analytically was chosen for the active control. This resonance frequency corresponds to mode (4,3), and has an anti-nodal line midway along the y direction. In the experiments, mode (4,3) is equivalent to the modeshape obtained at the resonance frequency of 222 Hz. Differences between the analytical and experimental results can be attributed to imperfections in the simply supported boundary conditions, some discrepancies in the values for the material properties, and equipment losses.

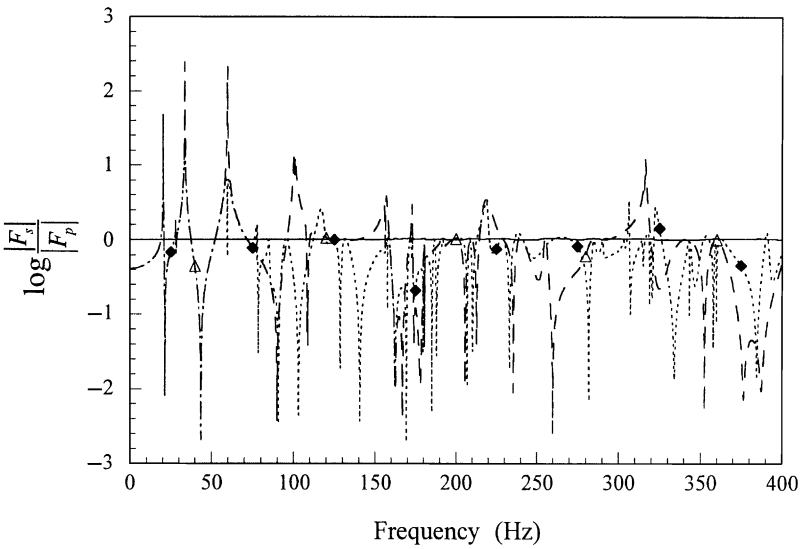

Fig. 4. Optimal control force amplitudes at fixed primary force and error sensor locations of (0.6,0.19) and (1.1,0.25), respectively, and control force locations of (0.8,0.19) (- - - - ◆ - - -), (0.6,0.25) ((– ≙ –)) and (0.6,0.31) (——).

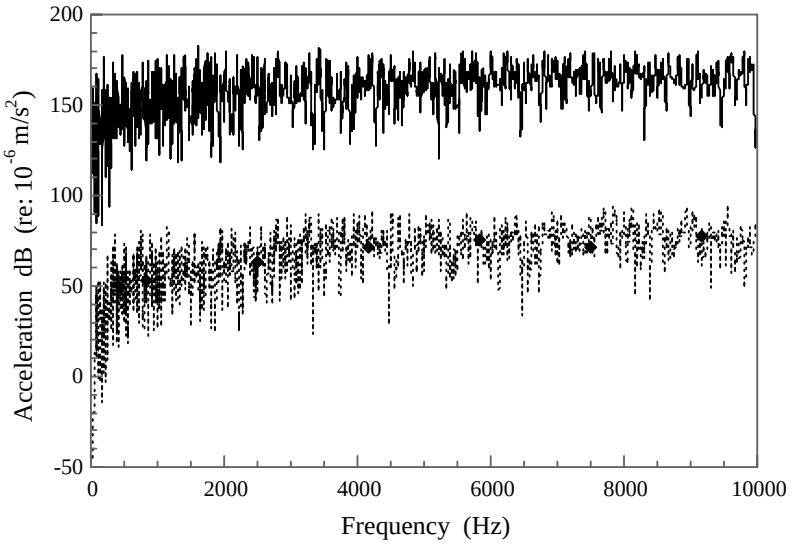

Fig. 5. Primary (——) and controlled acceleration distributions for single frequency control over a broad frequency range at the optimal control force and error sensor arrangement.

Table 1
Total kinetic energy levels of the controlled response for the single plate for various error sensor locations

Error sensor location (x_e, y_e)	Kinetic energy levels obtained analytically (N m)	Kinetic energy levels obtained experimentally (N m)
(0.8,0.25)	5.23×10^{-7}	6.42×10^{-7}
(0.6,0.25)	5.23×10^{-7}	6.70×10^{-7}
(0.8,0.19)	1.81×10^{-6}	1.06×10^{-6}
(0.8,031)	1.87×10^{-6}	1.09×10^{-6}
(1.2,0.1)	2.85×10^{-6}	1.55×10^{-6}

Table 1

Table 1 shows the total kinetic energy levels of the plate under the control application obtained analytically and experimentally for various error sensor locations. The primary and secondary shakers were positioned along the y direction at (0.6,0.19) and (0.6,0.31), respectively. Table 1 shows that better attenuation is achieved when the error sensor is located midway between the primary and secondary shakers at $y_e = 0.25$ m. The greatest attenuation (experimentally) occurs when the error sensor is downstream of the shakers, where the effects of any near-field disturbances are reduced.

Using the symmetrical control arrangement under single frequency control over a broad frequency range corresponding to $(x_p, y_p) = (0.6, 0.19)$, $(x_s, y_s) = (0.6, 0.31)$ and $(x_e, y_e) = (0.8, 0.25)$, the controlled plate response was obtained both analytically and experimentally for mode (4,3). Figs. 6(a) and (b) compare the uncontrolled and controlled acceleration distributions obtained analytically, whilst Figs. 7(a) and (b) show those obtained experimentally. In both cases, the controlled response was completely different to the uncontrolled response. Instead of two nodal lines in the y direction as shown in the modeshapes, the controlled responses shows only one

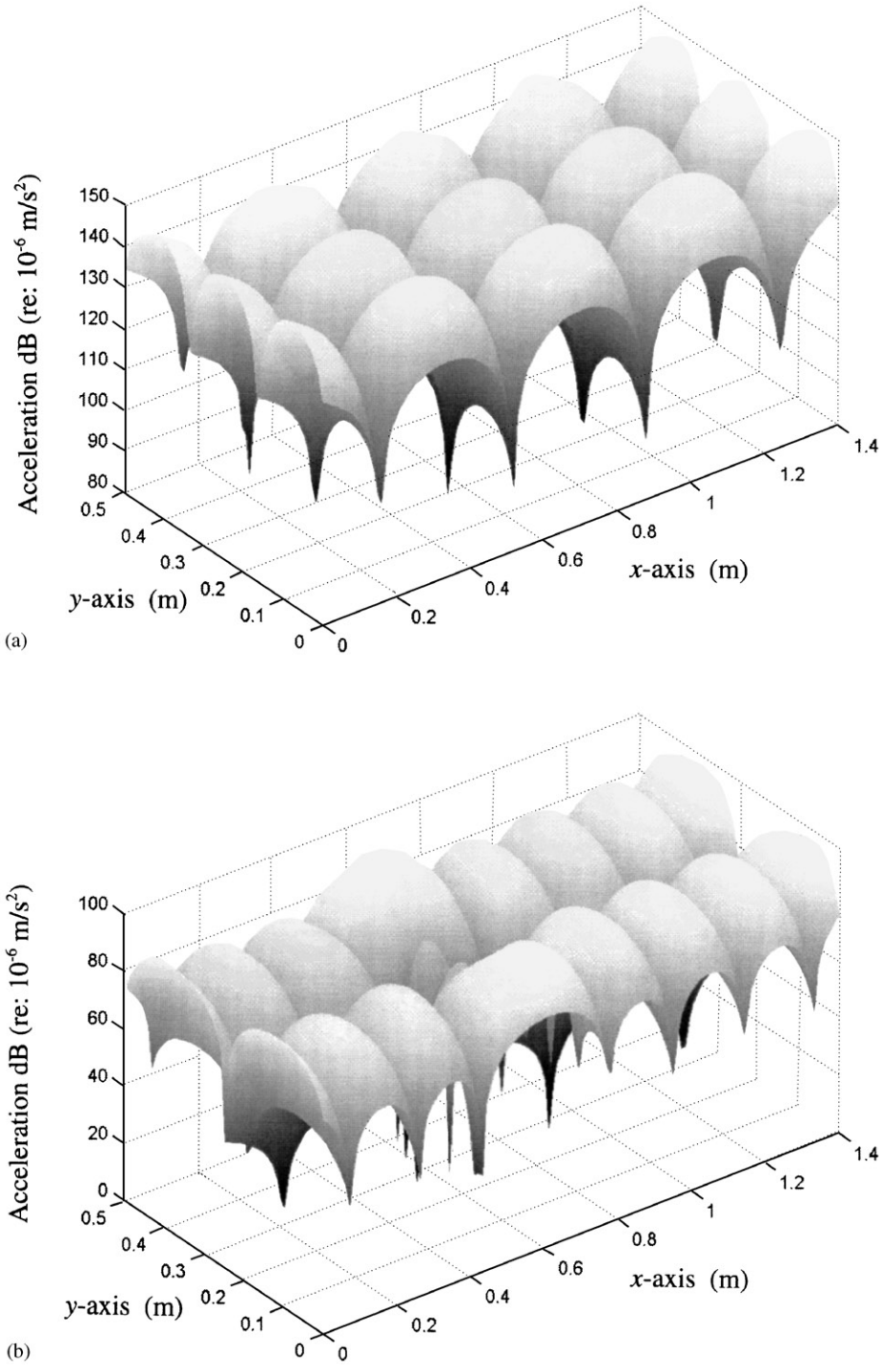

Fig. 6. Surfaces plots of (a) the modeshape at 209 Hz (analytical) corresponding to mode (4,3) and (b) the controlled response at 209 Hz and an error sensor location of (0.8,0.25).

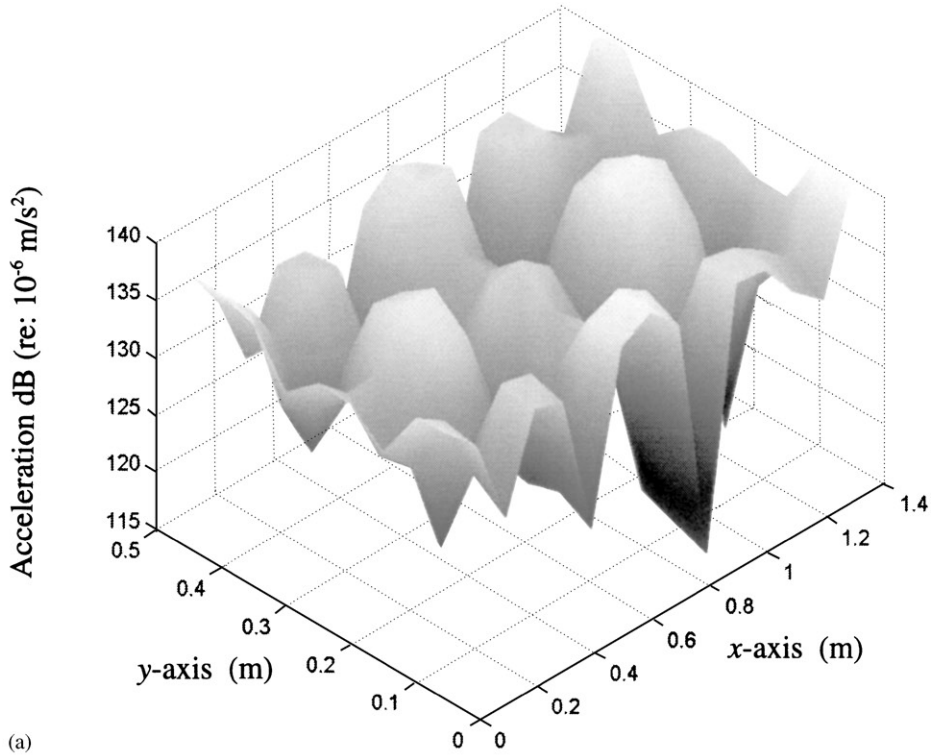

(a)

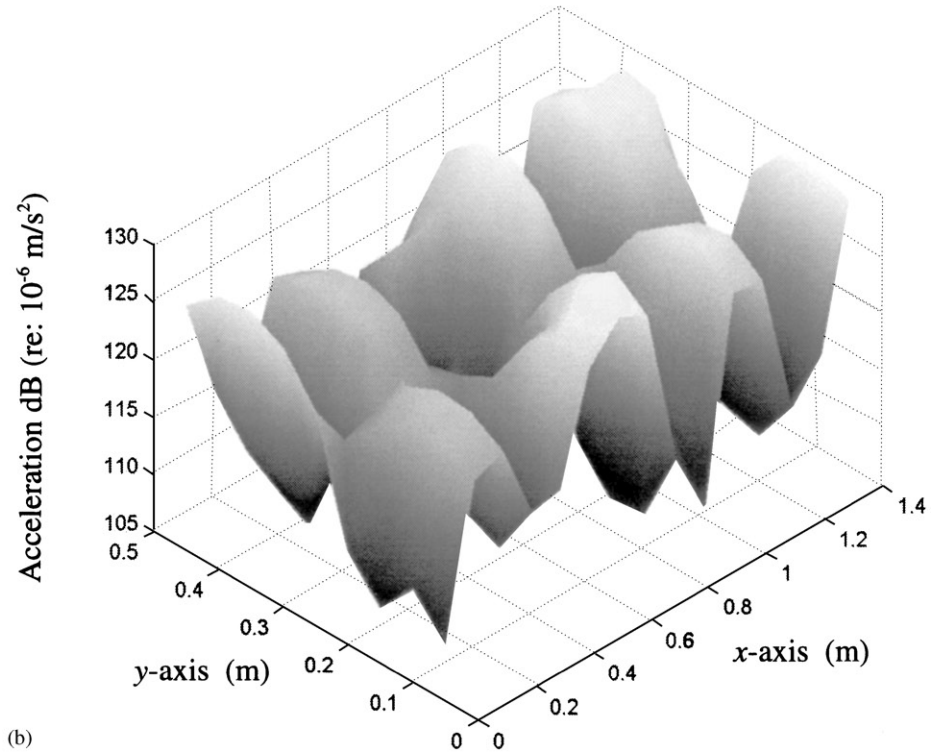

(b)

Fig. 7. Surface plots of (a) the plate at 222 Hz (experimental) corresponding to mode (4,3) and (b) the controlled response at 222 Hz and an error sensor location of (0.8,0.25).

nodal line along the same y direction as the error sensor. This error sensor location also corresponded to an anti-nodal point. Figs. 6 and 7 also show that global attenuation of the plate response for mode (4,3) has been achieved both theoretically and experimentally. This is attributed to the fact that the error sensor is located along an anti-nodal line of the primary response.

5.3. Single plate: single frequency control using multiple error sensors

The objective of using multiple error sensors was to determine if the control performance could be improved with the addition of extra sensors. The global reduction of the plate's kinetic energy was used as a measure to assess the control performance using multiple error sensors. From the theoretical results, no improvement in the control performance was achieved with the symmetrical control application, that is, with the control force in line with the primary force in the y direction, and the two error sensors located midway between the two shakers along the anti-nodal line of mode (4,3). In the experiments, if the first error sensor is optimally located, the second error sensor can improve the control performance if it is also located along the same anti-nodal line. The difference in the analytical and experimental results is due to the fact that in the analytical case, one error sensor is sufficient to attenuate the entire anti-nodal line. As a result, there is no signal for the second error sensor to control. In the experiments, the response along the anti-nodal line is not completely attenuated. Hence, a second error sensor will slightly improve the results. However, if the second error sensor is placed in an arbitrary location not corresponding to an anti-nodal line, the control performance was shown to deteriorate. This is due to the fact that the single control actuator must divide its effort between the two error signals such that the sum of the squared plate displacement for each error sensor location is minimised. Location of the error sensor on an anti-nodal line results in global control of the plate response. However, reducing the plate's response at the location of the second error sensor away from the anti-nodal line does not significantly contribute to the global reduction of the plate.

5.4. L-shaped plate: excitation and control at single frequencies over a broad frequency range

Due to the simply supported boundary conditions, the primary and control shakers were located in plate 1 in line with each other along the y direction at $(-0.8,0.19)$ and $(-0.8,0.31)$, respectively (the negative sign is due to the sign convention for the L-shaped plate). These shaker locations coincide with the shaker locations of the single plate. Several error sensor locations were examined. Fig. 8 shows the uncontrolled and controlled acceleration distributions at error sensor locations of (0.37,0.22) and (0.23,0.31) in plate 2. There is very little difference in the level of attenuation achieved when the error sensor is in line with either the primary or control forces in the x direction, that is, at $y_e = 0.19$ and 0.31. Fig. 9 shows the controlled responses when the error sensor is located midway between the primary and control shakers at $y_e = 0.25$ in both plates 1 and 2. This figure shows that when the control force and error sensor are positioned in a symmetrical arrangement with respect to the primary force location, that is, the control force is in line and symmetrical with the primary force in the y direction (in plate 1) and the error sensor located midway between the forces (in either plates 1 or 2), the control performance is both maximised and independent of the excitation frequency.

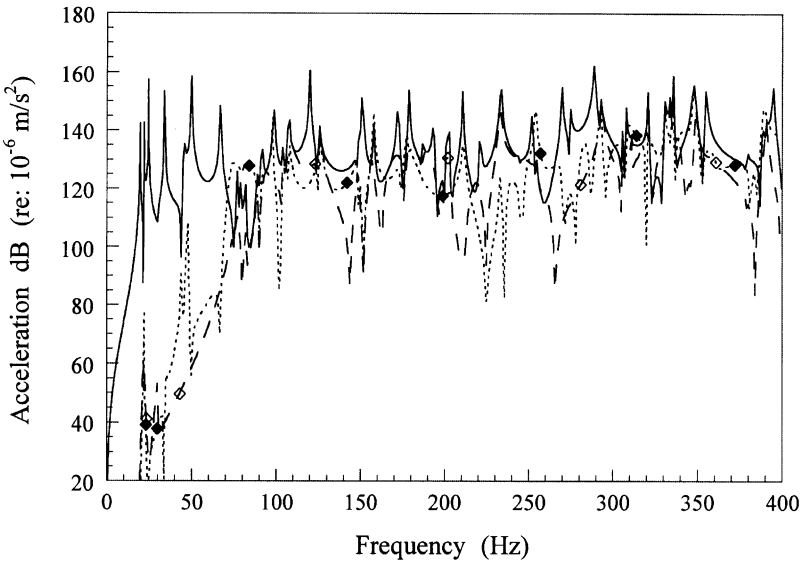

Fig. 8. Primary (——) and controlled acceleration distributions of the L-shaped plate for single frequency control over a broad frequency range at fixed primary and control force locations of (−0.8,0.19) and (−0.8,0.31), respectively, and error sensor locations of (0.37,0.22) (- - - - ◆ - - -) and (0.23,0.31) ((- ⋄ -)).

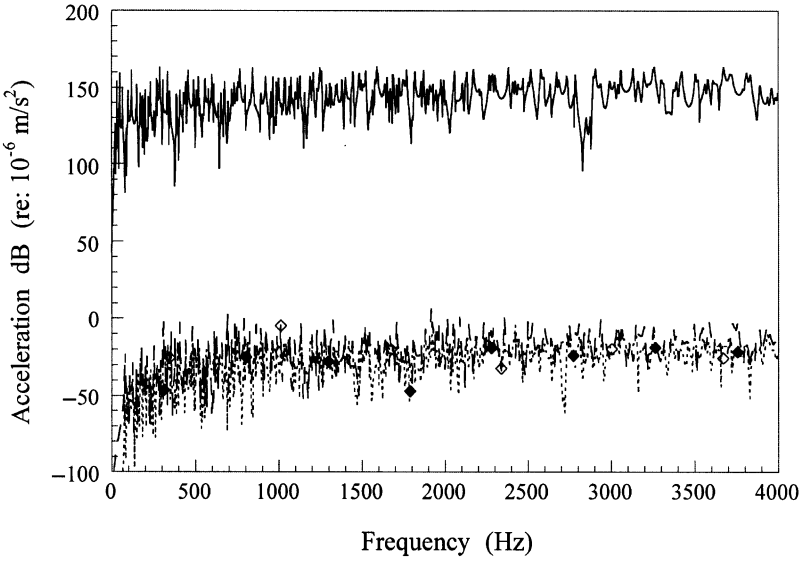

Fig. 9. Primary (——) and controlled acceleration distributions of the L-shaped plate for single frequency control over a broad frequency range at fixed primary and control force locations of (−0.8,0.19) and (−0.8,0.31), respectively, and error sensor locations of (0.23,0.25) (- - - - ◆ - - -) and (−0.6,0.25) ((- ⋄ -)).

5.5. L-shaped plate: single frequency control using a single error sensor

Two modes of vibration were examined for the L-shaped plate. The first mode has a similar modeshape to that of the single plate, with the anti-nodal line occurring along the width of the plate at $y = 0.25$ m. This corresponds to a resonance frequency of 244.9 Hz (analytically) and 247.8 Hz (experimentally). The second mode at a resonance frequency of 178.8 Hz (analytically) has a nodal line midway in the y direction. Figs. 10(a) and (b), respectively, show contour plots of the uncontrolled and controlled responses at 244.9 Hz, and an error sensor location of (0.3,0.25) in plate 2. At this error sensor location, the vibrational response of the L-shaped plate has been globally attenuated. As before with the single plate, two nodal lines along the x-axis of the modeshape have been replaced with a single nodal line along the same y location as the error sensor under the control application. Figs. 11(a) and (b) confirm the analytical results. Similar results were also obtained for the error sensor placed along the centreline at anti-nodal points in plate 1. Fig. 12(a) shows the contour plot of the modeshape at 178.8 Hz. In this case, there is only a single nodal line at $y = 0.25$ m. When the error sensor is located at (0.3,0.25) in plate 2, only attenuation of the nodal line occurs (Fig. 12(b)). However, when the single error sensor is located at an anti-nodal point of (0.17, 0.375), global attenuation of the L-shaped plate is achieved (Fig. 12(c)). Fig. 12(b) still confirms the results of the broadband frequency control, where under the symmetrical arrangement of the control application, attenuation at the error sensor location for all excitation frequencies is achieved. However, the symmetrical control application is obviously not suitable for global attenuation of the plates at a single resonance frequency.

5.6. L-shaped plate: single frequency control using multiple error sensors

The use of multiple error sensors was investigated to determine whether an improvement in the control performance could be achieved. For the single plate, it was shown that theoretically, there was no improvement in the control performance when a second optimally located error sensor was used in conjunction with a first optimally located error sensor. Experimentally, a slight improvement in the control performance was achieved using two optimally located error sensors. These results were also confirmed for the L-shaped plate. Table 2 shows the kinetic energy levels of the controlled response obtained experimentally at a resonance frequency of 247.8 Hz, using single and multiple error sensors on the L-shaped plate. As seen in Table 2, there is a slight increase in the control performance when two error sensors are located along the centreline (resulting in two optimally located error sensors), and a decrease in the control performance when the second error sensor is arbitrarily located.

6. Conclusions

In this paper, active attenuation of the plate vibration was both analytically and experimentally presented. Due to the simply supported and free boundary conditions, the mathematical modelling was based on a combination of a travelling wave solution and a modal solution. For point force excitation of both a single and L-shaped plate, the results obtained from the analytical model was found to agree very well with those obtained experimentally. Under single frequency

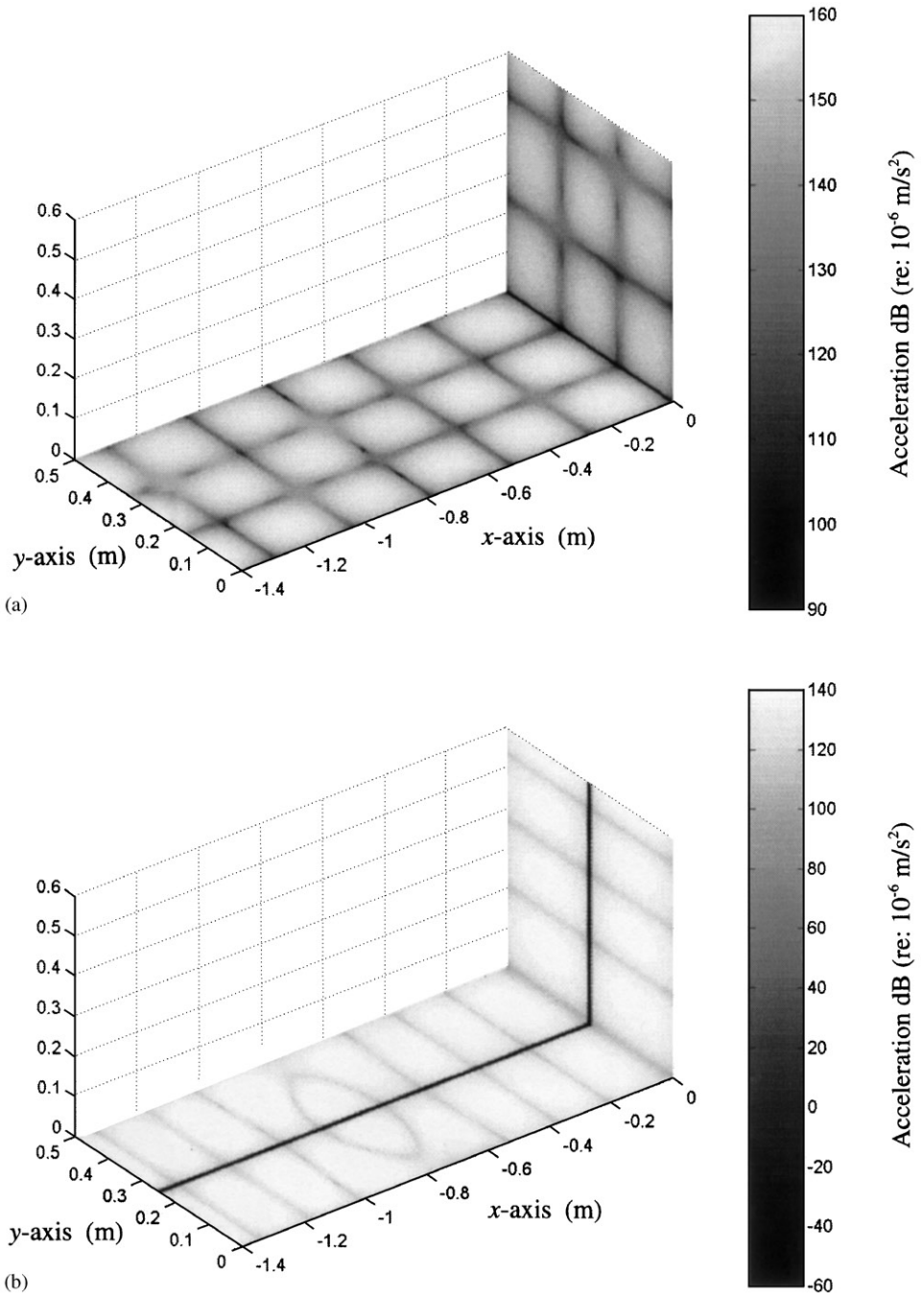

Fig. 10. Contour plots of (a) the modeshape at 244.9 Hz (analytical) and (b) the controlled response at 244.9 Hz and an error sensor location of (0.3,0.25) in plate 2.

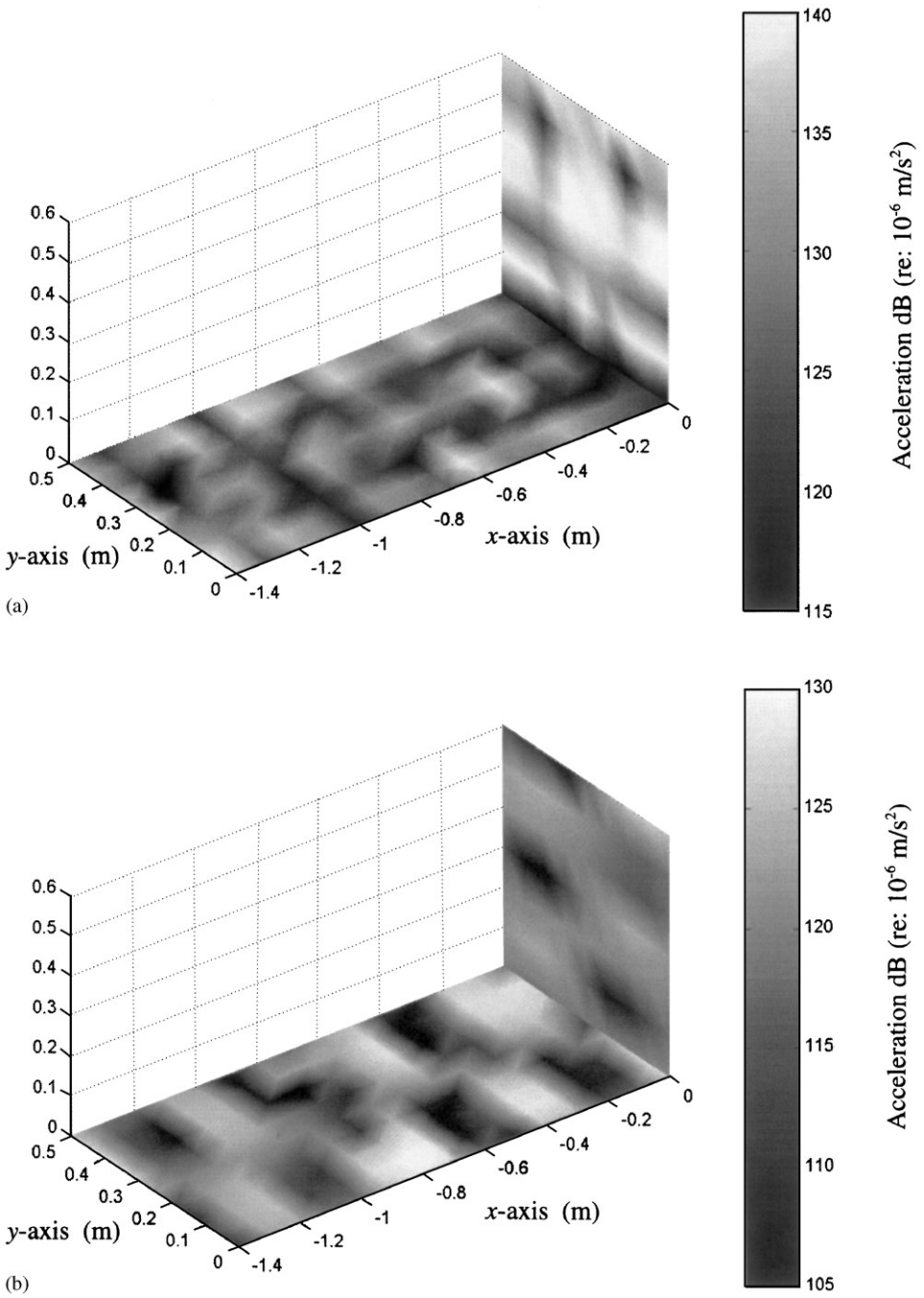

Fig. 11. Contour plots of (a) the modeshape at 247.8 Hz (experimental) and (b) the controlled response at 247.8 Hz and an error sensor location of (0.3,0.25) in plate 2.

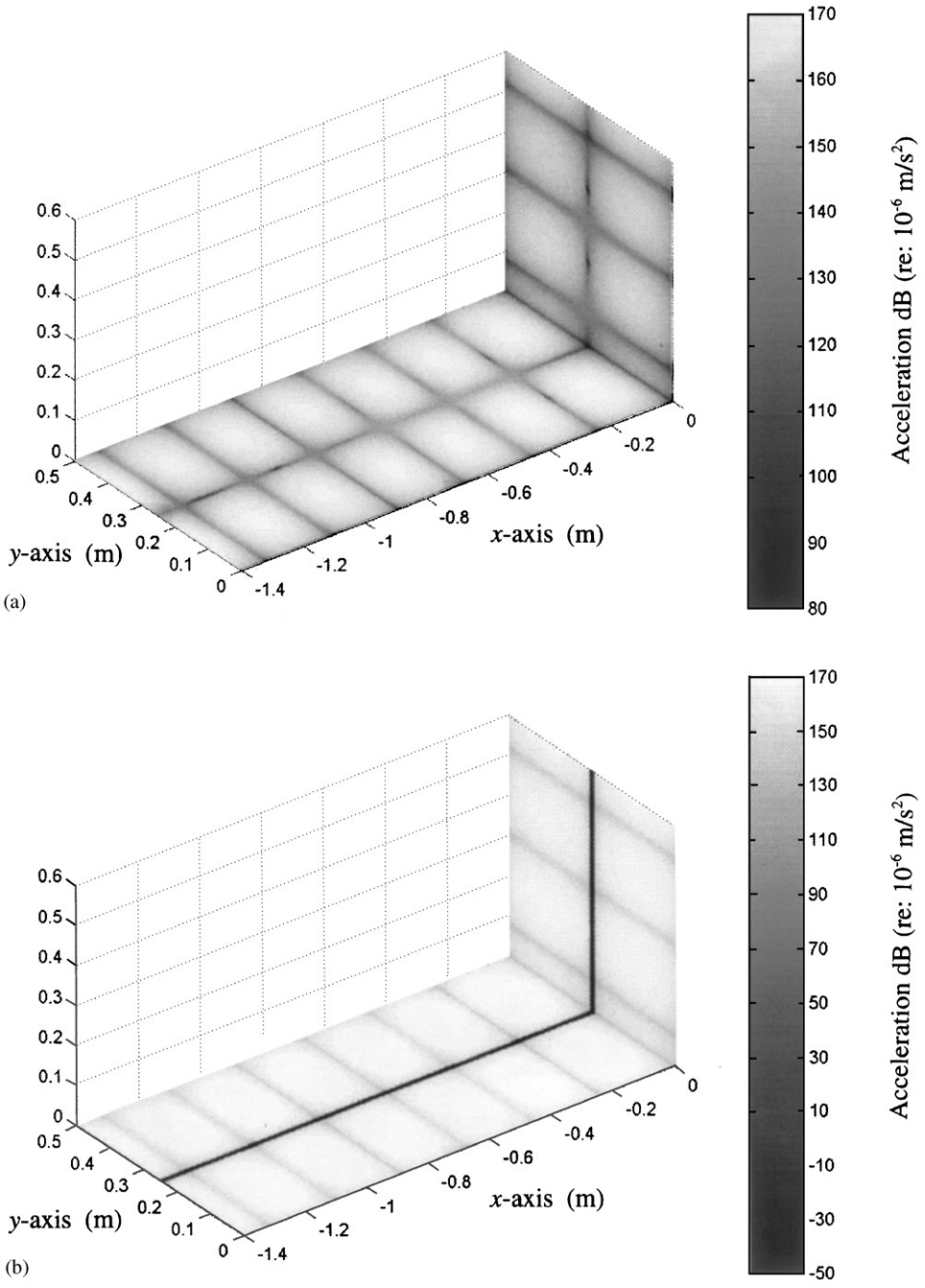

Fig. 12. Contour plots of (a) the modeshape at 178.8 Hz (analytical); (b) the controlled response at 178.8 Hz and an error sensor location of (0.3,0.25) in plate 2; and (c) the controlled response at 178.8 Hz and an error sensor location of (0.3,0.31) in plate 2.

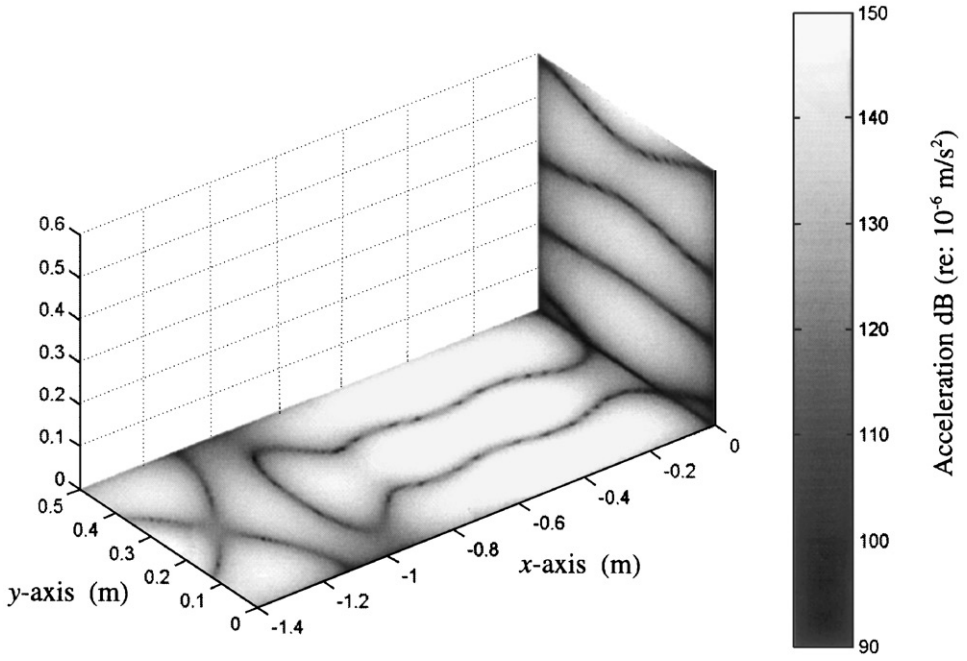

Fig. 12 (*continued*).

Table 2
Total kinetic energy levels of the controlled response for the L-shaped plate for using single and multiple error sensors

Single error sensor location	Kinetic energy levels (Nm)
(0.3,0.25)	1.23×10^{-7}
(0.3,0.31)	2.01×10^{-7}
(0.5,0.1)	2.86×10^{-7}
(−0.6,0.25)	1.27×10^{-7}
Multiple error sensor locations	
(−0.6,0.25) and (0.3,0.25)	9.90×10^{-8}
(−0.3,0.1) and (0.3,0.25)	3.27×10^{-7}

Table 2
Total kinetic energy levels of the controlled response for the L-shaped plate for using single and multiple error sensors

control in a broad frequency range, the control approach consisted of optimising both the control force and error sensor locations with respect to the primary force location. The optimal arrangement resulted in significant attenuation at all excitation frequencies. In addition, the amplitude ratio of the control force to the primary force is unity for all frequencies. Under single frequency control to examine the global response of the plate, the nodal lines of the plate response at a single resonance frequency significantly affected the control performance. Using a single, properly located error sensor, global attenuation of both the single plate and the L-shaped plate was achieved.

Acknowledgements

The authors would like to thank Dr. Eric Lawrey for his assistance with the Matlab programming to generate the L-shaped plate figures.

Appendix A

$$[\alpha] = \begin{bmatrix} -k_x^2 - \upsilon k_y^2 & -k_x^2 - \upsilon k_y^2 & k_n^2 - \upsilon k_y^2 & k_n^2 - \upsilon k_y^2 \\ \mathrm{j}k_x(k_x^2 + (2-\upsilon)k_y^2) & -\mathrm{j}k_x(k_x^2 + (2-\upsilon)k_y^2) & -k_n(k_n^2 - (2-\upsilon)k_y^2) & k_n(k_n^2 - (2-\upsilon)k_y^2) \\ 0 & 0 & 0 & 0 \\ 0 & 0 & 0 & 0 \\ \mathrm{e}^{-\mathrm{j}k_x x_p} & \mathrm{e}^{\mathrm{j}k_x x_p} & \mathrm{e}^{-k_n x_p} & \mathrm{e}^{k_n x_p} \\ -\mathrm{j}k_x \mathrm{e}^{-\mathrm{j}k_x x_p} & \mathrm{j}k_x \mathrm{e}^{\mathrm{j}k_x x_p} & -k_n \mathrm{e}^{-k_n x_p} & k_n \mathrm{e}^{k_n x_p} \\ -k_x^2 \mathrm{e}^{-\mathrm{j}k_x x_p} & -k_x^2 \mathrm{e}^{\mathrm{j}k_x x_p} & k_n^2 \mathrm{e}^{-k_n x_p} & -k_n^2 \mathrm{e}^{k_n x_p} \\ \mathrm{j}k_x^3 \mathrm{e}^{-\mathrm{j}k_x x_p} & -\mathrm{j}k_x^3 \mathrm{e}^{\mathrm{j}k_x x_p} & -k_n^3 \mathrm{e}^{-k_n x_p} & k_n^3 \mathrm{e}^{k_n x_p} \end{bmatrix}$$

$$\begin{bmatrix} 0 & 0 & 0 & 0 \\ 0 & 0 & 0 & 0 \\ (-k_x^2 - \upsilon k_y^2)\mathrm{e}^{-\mathrm{j}k_x L_x} & (-k_x^2 - \upsilon k_y^2)\mathrm{e}^{\mathrm{j}k_x L_x} & (k_n^2 - \upsilon k_y^2)\mathrm{e}^{-k_n L_x} & (k_n^2 - \upsilon k_y^2)\mathrm{e}^{k_n L_x} \\ \mathrm{j}k_x(k_x^2 + (2-\upsilon)k_y^2)\mathrm{e}^{-\mathrm{j}k_x L_x} & -\mathrm{j}k_x(k_x^2 + (2-\upsilon)k_y^2)\mathrm{e}^{\mathrm{j}k_x L_x} & -k_n(k_n^2 - (2-\upsilon)k_y^2)\mathrm{e}^{-k_n L_x} & k_n(k_n^2 - (2-\upsilon)k_y^2)\mathrm{e}^{k_n L_x} \\ -\mathrm{e}^{-\mathrm{j}k_x x_p} & -\mathrm{e}^{\mathrm{j}k_x x_p} & -\mathrm{e}^{-k_n x_p} & -\mathrm{e}^{k_n x_p} \\ \mathrm{j}k_x \mathrm{e}^{-\mathrm{j}k_x x_p} & -\mathrm{j}k_x \mathrm{e}^{\mathrm{j}k_x x_p} & k_n \mathrm{e}^{-k_n x_p} & -k_n \mathrm{e}^{k_n x_p} \\ k_x^2 \mathrm{e}^{-\mathrm{j}k_x x_p} & k_x^2 \mathrm{e}^{\mathrm{j}k_x x_p} & -k_n^2 \mathrm{e}^{-k_n x_p} & k_n^2 \mathrm{e}^{k_n x_p} \\ -\mathrm{j}k_x^3 \mathrm{e}^{-\mathrm{j}k_x x_p} & \mathrm{j}k_x^3 \mathrm{e}^{\mathrm{j}k_x x_p} & k_n^3 \mathrm{e}^{-k_n x_p} & -k_n^3 \mathrm{e}^{k_n x_p} \end{bmatrix}.$$

Appendix B

$$
[\alpha] = \begin{bmatrix}
(-k_{x1}^2 - \upsilon k_y^2)\mathrm{e}^{-\mathrm{j}k_{x1}L_{x1}} & (-k_{x1}^2 - \upsilon k_y^2)\mathrm{e}^{\mathrm{j}k_{x1}L_{x1}} & (k_{n1}^2 - \upsilon k_y^2)\mathrm{e}^{-k_{n1}L_{x1}} & (k_{n1}^2 - \upsilon k_y^2)\mathrm{e}^{k_{n1}L_{x1}} & 0 & 0 \\
\mathrm{j}k_{x1}(k_{x1}^2 + (2-\upsilon)k_y^2)\mathrm{e}^{-\mathrm{j}k_{x1}L_{x1}} & -\mathrm{j}k_{x1}(k_{x1}^2 + (2-\upsilon)k_y^2)\mathrm{e}^{\mathrm{j}k_{x1}L_{x1}} & -k_{n1}(k_{n1}^2 - (2-\upsilon)k_y^2)\mathrm{e}^{-k_{n1}L_{x1}} & k_{n1}(k_{n1}^2 - (2-\upsilon)k_y^2)\mathrm{e}^{k_{n1}L_{x1}} & 0 & 0 \\
0 & 0 & 0 & 0 & 0 & 0 \\
0 & 0 & 0 & 0 & 0 & 0 \\
\mathrm{e}^{-\mathrm{j}k_{x1}x_p} & \mathrm{e}^{\mathrm{j}k_{x1}x_p} & \mathrm{e}^{-k_{n1}x_p} & \mathrm{e}^{k_{n1}x_p} & -\mathrm{e}^{-\mathrm{j}k_{x1}x_p} & -\mathrm{e}^{\mathrm{j}k_{x1}x_p} \\
-\mathrm{j}k_{x1}\mathrm{e}^{-\mathrm{j}k_{x1}x_p} & \mathrm{j}k_{x1}\mathrm{e}^{\mathrm{j}k_{x1}x_p} & -k_{n1}\mathrm{e}^{-k_{n1}x_p} & k_{n1}\mathrm{e}^{k_{n1}x_p} & \mathrm{j}k_{x1}\mathrm{e}^{-\mathrm{j}k_{x1}x_p} & -\mathrm{j}k_{x1}\mathrm{e}^{\mathrm{j}k_{x1}x_p} \\
-k_{x1}^2\mathrm{e}^{-\mathrm{j}k_{x1}x_p} & -k_{x1}^2\mathrm{e}^{\mathrm{j}k_{x1}x_p} & k_{n1}^2\mathrm{e}^{-k_{n1}x_p} & k_{n1}^2\mathrm{e}^{k_{n1}x_p} & k_{x1}^2\mathrm{e}^{-\mathrm{j}k_{x1}x_p} & k_{x1}^2\mathrm{e}^{\mathrm{j}k_{x1}x_p} \\
\mathrm{j}k_{x1}^3\mathrm{e}^{-\mathrm{j}k_{x1}x_p} & -\mathrm{j}k_{x1}^3\mathrm{e}^{\mathrm{j}k_{x1}x_p} & -k_{n1}^3\mathrm{e}^{-k_{n1}x_p} & k_{n1}^3\mathrm{e}^{k_{n1}x_p} & -\mathrm{j}k_{x1}^3\mathrm{e}^{-\mathrm{j}k_{x1}x_p} & \mathrm{j}k_{x1}^3\mathrm{e}^{\mathrm{j}k_{x1}x_{op}} \\
0 & 0 & 0 & 0 & -k_{x1}^2 & -k_{x1}^2 \\
0 & 0 & 0 & 0 & -\mathrm{j}k_{x1} & \mathrm{j}k_{x1} \\
0 & 0 & 0 & 0 & \mathrm{j}(k_{x1}^3 - k_p^4/k_L) & -\mathrm{j}(k_{x1}^3 + k_p^4/k_L) \\
0 & 0 & 0 & 0 & 0 & 0
\end{bmatrix}
$$

$$
\begin{bmatrix}
0 & 0 & 0 & 0 & 0 & 0 \\
0 & 0 & 0 & 0 & 0 & 0 \\
0 & 0 & (-k_{x2}^2 - \upsilon k_y^2)\mathrm{e}^{-\mathrm{j}k_{x2}L_{x2}} & (-k_{x2}^2 - \upsilon k_y^2)\mathrm{e}^{\mathrm{j}k_{x2}L_{x2}} & (k_{n2}^2 - \upsilon k_y^2)\mathrm{e}^{-k_{n2}L_{x2}} & (k_{n2}^2 - \upsilon k_y^2)\mathrm{e}^{k_{n2}L_{x2}} \\
0 & 0 & \mathrm{j}k_{x2}(k_{x2}^2 + (2-\upsilon)k_y^2)\mathrm{e}^{-\mathrm{j}k_{x2}L_{x2}} & -\mathrm{j}k_{x2}(k_{x2}^2 + (2-\upsilon)k_y^2)\mathrm{e}^{\mathrm{j}k_{x2}L_{x2}} & -k_{n2}(k_{n2}^2 - (2-\upsilon)k_y^2)\mathrm{e}^{-k_{n2}L_{x2}} & k_{n2}(k_{n2}^2 - (2-\upsilon)k_y^2)\mathrm{e}^{k_{n2}L_{x2}} \\
-\mathrm{e}^{-k_{n1}x_o} & -\mathrm{e}^{k_{n1}x_o} & 0 & 0 & 0 & 0 \\
k_{n1}\mathrm{e}^{-k_{n1}x_o} & -k_{n1}\mathrm{e}^{k_{n1}x_o} & 0 & 0 & 0 & 0 \\
-k_{n1}^2\mathrm{e}^{-k_{n1}x_o} & -k_{n1}^2\mathrm{e}^{k_{n1}x_o} & 0 & 0 & 0 & 0 \\
k_{n1}^3\mathrm{e}^{-k_{n1}x_o} & -k_{n1}^3\mathrm{e}^{k_{n1}x_o} & 0 & 0 & 0 & 0 \\
k_{n1}^2 & k_{n1}^2 & k_{x2}^2 & k_{x2}^2 & -k_{n2}^2 & -k_{n2}^2 \\
-k_{n1} & k_{n1} & \mathrm{j}k_{x2} & -\mathrm{j}k_{x2} & k_{n2} & -k_{n2} \\
-(k_{n1}^3 + \mathrm{j}k_p^4/k_L) & (k_{n1}^3 - \mathrm{j}k_p^4/k_L) & 0 & 0 & 0 & 0 \\
0 & 0 & \mathrm{j}(k_{x2}^3 + k_p^4/k_L) & -\mathrm{j}(k_{x2}^3 - k_p^4/k_L) & -(k_{n2}^3 - \mathrm{j}k_p^4/k_L) & (k_{n2}^3 + \mathrm{j}k_p^4/k_L)
\end{bmatrix}.
$$

References

[1] X. Pan, C.H. Hansen, Active control of vibratory power transmission along a semi-infinite plate, Journal of Sound and Vibration 184 (1995) 585–610.
[2] R.L. Clark, C.R. Fuller, Optimal placement of piezoelectric actuators and polyvinylidene fluoride error sensors in active structural acoustic control approaches, Journal of the Acoustical Society of America 92 (1992) 1521–1533.
[3] C. Guigou, C.R. Fuller, K.D. Frampton, Experiments on active control of acoustic radiation due to a clamped edge on a semi-infinite beam, Journal of Sound and Vibration 169 (1994) 503–526.
[4] K.H. Baek, S.J. Elliott, Natural algorithms for choosing source locations in active control systems, Journal of Sound and Vibration 186 (1995) 245–267.
[5] P. De Fonseca, P. Sas, H. Van Brussel, A comparative study of methods for optimising sensor and actuator locations in active control applications, Journal of Sound and Vibration 221 (1999) 651–679.
[6] C. Boisson, J.L. Guyader, P. Millot, C. Lesueur, Energy transmission in finite coupled plates, Part II: application to an L-shaped structure, Journal of Sound and Vibration 81 (1982) 93–105.
[7] R.C.N. Leung, R.J. Pinnington, Wave propagation through right-angled joints with compliance-flexural incident wave, Journal of Sound and Vibration 142 (1990) 31–46.
[8] J.M. Cuschieri, M.D. McCollum, In-plane and out-of-plane waves' power transmission through an L-plate junction using the mobility power flow approach, Journal of the Acoustical Society of America 100 (1996) 857–870.
[9] N.J. Kessissoglou, Active attenuation of the wave transmission through an L-plate junction, Journal of the Acoustical Society of America 110 (2001) 267–277.
[10] A.W. Leissa, Vibrations of Plates, American Institute of Physics, Woodbury, NY, 1993.
[11] C.R. Fuller, S.J. Elliott, P.A. Nelson, Active Control of Vibration, Academic Press, London, 1996.
[12] N. Farag, Comparison of Vibration Properties of Flat Panels of Various Forms of Construction, Master of Science Thesis, Cranfield Institute of Technology, 1979.
[13] S.D. Snyder, G. Vokalek, EZ-ANC User's Guide, Causal Systems Pty Ltd, 1994.